Iron-based Polyanionic Cathodes for Sustainable Sodium-Ion Batteries

Project Report (Final)

Summary of Results

Metal-ion doping (Mn^{2+}, Ni^{2+}, Zn^{2+}, K^{+}) and reduced graphene oxide (rGO) incorporation into the $Na_4Fe_3(PO_4)_2(P_2O_7)$ (NFPP) structure were successfully achieved using a conventional sol–gel synthesis method followed by calcination. These modifications led to improved phase purity, better morphology, and significantly enhanced electrochemical performance. The partial substitution of Fe with Mn^{2+} and Ni^{2+}, as well as the replacement of Na^{+} with K^{+}, likely introduced structural vacancies, which appear to suppress the formation of the electrochemically inactive maricite (m-$NaFePO_4$) phase. These structural changes may to improved Na^{+} insertion and extraction kinetics, potentially by facilitating ion transport and reducing migration barriers.

Among the synthesized materials, 0.05 Mn-doped NFPP (0.05 Mn-NFPP) demonstrated the best overall electrochemical performance. Introduction of approximately 10% Fe and 1% Na vacancies is believed to have contributed to the suppression of m-$NaFePO_4$ formation, a possible narrowing of the band gap, and improved Na^{+} ion mobility. This material exhibited improved specific capacity, rate capability, and long-term cycling stability compared to pristine NFPP cathode. Cyclic voltammetry (CV) at various scan rates further supported enhanced Na^{+} diffusion kinetics and increased electrochemical reversibility following Mn^{2+} doping. In comparison, 0.1 Ni-doped NFPP (0.1 Ni-NFPP) achieved the highest phase purity and performed well at low C-rates, but showed inferior capacity at higher rates. Ex-situ X-ray absorption spectroscopy (XAS) revealed that doping induced lattice distortions, with Ni causing the least distortion among the dopants tested. These results suggest that maintaining low doping levels is critical for preserving the structural integrity of NFPP. All doped and undoped NFPP samples exhibited highly reversible changes in the Fe–O coordination environment and bond lengths, consistent with a Fe^{2+}/Fe^{3+} redox mechanism during cycling. Fe L-edge XAS confirmed that both Mn- and Ni-doped NFPP materials undergo redox cycling predominantly between Fe^{2+} and near Fe^{3+}. Additionally, O K-edge XAS measurements indicated that Fe–O hybridization was strongest in the Mn-doped sample across both charged and discharged states, which may correlate with its superior electrochemical behavior. In contrast, minimal amount of Zn^{2+} doping strategy led to capacity fade, likely due to the higher content of electrochemically inactive m-$NaFePO_4$ and $Na_2ZnP_2O_7$ phases, as well as associated lattice distortions.

Additionally, K^{+} doping at Na sites within NFPP structure significantly enhanced the electrochemical performance compared other doped compounds reported in this study, with K0.02-NFPP achieving a maximum reversible capacity of 98.31 mAh g^{-1} (vs. Na/Na^{+}) at 0.1 C within a potential window of 1.8–3.8 V. Long-term cycling tests demonstrated excellent stability, with the material retaining 98.07% of its initial capacity over 1000 cycles. Furthermore, RGO coating on the surface of K^{+}-doped NFPP nanoparticles improved rate capability without significant capacity fade at high C-rates, indicating likely improved electronic conductivity. The combined effects of K^{+} doping and rGO coating appear to have suppressed m-$NaFePO_4$ phase formation and improved particle size uniformity and porosity, thereby enhancing electronic and ionic transport. These strategies present a promising approach for developing high-performance cathode materials for next-generation sodium-ion batteries. Two scientific articles are planned to be published based on this work.

1. Introduction

A total of 450 kSEK was granted by Åforsk to Uppsala University to support the development of a stable, low-cost, and sustainable cathode material for sodium-ion batteries (SIBs), using an iron-based polyanionic compound, $Na_4Fe_3(PO_4)_2(P_2O_7)$ (NFPP). The primary objective of the project is to achieve enhanced phase purity and morphological control through metal-ion doping and carbon-based surface modification, with the goal of improving both short-range and long-range electronic conductivity.

$Na_4Fe_3(PO_4)_2(P_2O_7)$ (NFPP) has recently emerged as a promising SIB cathode owing to its robust framework, three-dimensional Na^+ diffusion channels, favorable theoretical capacity (~129 mAh g^{-1}), and a stable voltage plateau (~3.1 V vs. Na^+/Na) [1]. Despite these advantages, NFPP suffers from inherently low electronic conductivity, sluggish Na^+ kinetics, and formation of electrochemically inactive m-$NaFePO_4$ impurity during the synthesis, all of limit its practical application [2]. Carbon coating has emerged as an effective strategy to enhance surface-level electronic conductivity and to mitigate nanoparticle agglomeration, contributing to the improved rate capability and cycling stability. However, many commonly used carbon sources as carbon nanotubes (CNTs) and graphene, are costly and may compromise overall energy density due to their electrochemically inactive nature when present in excess [3]. Therefore, developing cost-effective simplified synthesis routes that minimize processing steps is essential for advancing more sustainable cathode materials. While carbon additives can enhance electronic conductivity externally, they do not resolve the intrinsic limitations of the active NFPP material. To address this, metal-ion doping has been explored to as a means to alter the internal structure and improve electrochemical performance. Doping is believed to introduce impurity energy states, which may help reduce the electronic band gap and lower the energy barrier for Na^+ ion migration. In addition, dopant-induced lattice modifications are thought to subtly affect Na^+ transport pathways, potentially facilitating more efficient ion insertion and extraction during operation [4].

Our approach involves improving the purity and crystal structure of NFPP through targeted metal-ion doping and the incorporation of reduced graphene oxide (rGO) to serve as a conductive network. This is expected to enhance both mechanical integrity and electronic connectivity. NFPP composites doped with Mn^{2+}, Ni^{2+}, Zn^{2+}, and K^+ were synthesized via a traditional sol-gel process followed by low temperature calcination. These modifications are intended to regulate Fe/Na site occupancy, expand lattice parameters, and potentially enhance Na^+ transport. To characterize the materials, advanced characterization techniques including as X-ray diffraction (XRD), field emission scanning electron microscopy (FE-SEM), transmission electron microscopy (TEM), and energy-dispersive X-ray spectroscopy (EDX) were employed to evaluate morphology and phase composition. Electrochemical properties were assessed using galvanostatic cycling and cyclic voltammetry in half-cell configurations. Additionally, ex-situ X-ray absorption spectroscopy (XAS) and resonant inelastic X-ray scattering (RIXS) were used to investigate oxidation state changes and sodium storage mechanisms during cycling.

2. Experimental Methods

2.1 Synthesis of $Na_4Fe_{3-x}M_x(PO_4)_2(P_2O_7)$

$Na_4Fe_{3-x}M_x(PO_4)_2(P_2O_7)$ (M: Mn, Ni, or Zn) (x = 0, 0.01, 0.03, 0.05, 0.1, 0.2 and 0.4) precursors were synthesized by a simple sol-gel process using $Fe(NO_3)_3{\cdot}9H_2O$ (Thermo Fisher, ≥99.9995%), $Mn(NO_3)_2{\cdot}xH_2O$ (Sigma-Aldrich, ≥99.999%), $Ni(NO_3)_2{\cdot}6H_2O$ (Sigma-Aldrich, ≥99.999%), $Zn(NO_3)_3{\cdot}6H_2O$ (Sigma-Aldrich, ≥99.9995%), ascorbic acid ($C_6H_8O_6$) (Sigma-Aldrich, ≥99), $NaH_2PO_4.2H_2O$ (Sigma-Aldrich, ≥98) and citric acid ($C_6H_8O_7$) (Sigma-Aldrich, ≥99.5) as raw materials. First, stoichiometric amount of $Fe(NO_3)_3{\cdot}9H_2O$ as Fe^{3+} precursor was dissolved in 50 mL distilled water at room temperature and was converted into Fe^{2+} state by the addition of a pinch of ascorbic acid

($C_6H_8O_6$) resulting a color change from brown to colorless jade-green [5]. Secondly, stoichiometric amount of dopant (Mn, Ni, Zn) was added to the above solution. After that, 0.02 mol $NaH_2PO_4.2H_2O$ was added into solution and stirred until dissolution at room temperature. Finally, the required amount of citric acid was added to the mixture as a chelating agent and carbon source. The resultant solution was then mixed in an oil bath at 80 ℃ until gel formation. After the evaporation of excess water, the precursor powder was dried in a vacuum oven at 120 ℃ overnight. Next, the dried metal-citro-nitrate complex gel was pressed into cylindrical pellets, which herein after may be referred as sol-gel precursor pellets. Precursor pellets were pre-calcinated at 300 ℃ for 5 h under Ar or Ar/H_2 gas (95:5 vol.%) flow with a heating rate of 3 ℃ min^{-1} to eliminate organic components. Finally, the amorphous intermediate products obtained after pre-calcination, respectively, were ground in an agate mortar and pelletized again using a disc-shaped mold (⌀ = 13 mm). The pellets of intermediate compounds were further annealed at 500 ℃ for 10 h under flowing Ar or Ar/H_2 gas (95:5 vol.%) with a heating rate of 3 ℃ min^{-1}. During the calcination, carbonaceous sources are thermally decomposed to form an in situ amorphous carbon coating (CC) layer on the NFPP surface. After naturally cooling down to room temperature, nanosized Mn-NFPP/CC, Ni-NFPP/CC, Zn-NFPP/CC cathodes were obtained.

2.2 Synthesis of K^+ doped $Na_{4-x}K_xFe_3(PO_4)_2(P_2O_7)$@rGO Composite

$Na_{4-x}K_xFe_3(PO_4)_2(P_2O7)$ (NFPP) materials were synthesized via a citric acid-assisted sol-gel method, with potassium doping levels of x = 0.01, 0.02, 0.05, and 0.08. These samples are referred to as K0.01-NFPP/CC, K0.02-NFPP/CC, K0.05-NFPP/CC, and K0.08-NFPP/CC, respectively. 0.015 mol $Fe(NO_3)_3.9H_2O$ was dissolved in 50 mL of deionized water and a pinch of ascorbic acid was gradually added to the solution, which was stirred for 1 hour until a homogenous colorless jade-green solution was formed. Subsequently, $NaH_2PO_4{\cdot}2H_2O$, KNO_3, and citric acid were added according to the molar ratios. For the synthesis of NFPP, incorporated reduced graphene oxide (then was labeled with K0.02-NFPP@rGO) followed the same method, however, 0.25 g of graphene oxide (GO) was added and the amount of citric acid was reduced to 1.7377 g. The mixed solution was heated in silicon oil bath at 80 ℃ until a brownish gel was formed. The formed gel was transferred to the Buchi oven and dried at 120 ℃ overnight under applied vacuum to remove the excess water, yielding a dry precursor powder. The powder was then pressed into 13 mm diameter cylindrical pellets using a steel mold and subjected to a two-step calcination process: First, pre-calcination was carried out at 300 ℃ under Ar/H_2 (95:5 vol.%) for 5 h to remove the organic residues from citric and nitric precursors. Then, the calcination process was performed at 500 ℃ for 10 h under the same gas flow, using a heating rate of 3 ℃ min^{-1}, to promote crystallization and NFPP phase formation. The schematic illustration of K^+-doped NFPP synthesis process is shown in **Figure 1**.

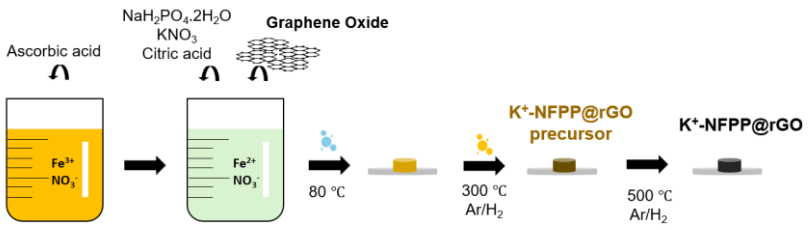

Figure 1. Schematic illustration for the synthesis of K^+ doped-NFPP@rGO

2.3 Battery Preparation

Electrodes were fabricated by mixing the active material with conductive carbon black (C-ENERGY Super C65, Imerys) and polyvinylidene fluoride (PVDF) (Kynar HSV 900) binder in an 80:10:10 weight

ratio using N-methyl-2-pyrrolidone (NMP) (Sigma-Aldrich®) as the solvent. Electrode slurry was cast onto carbon-coated aluminum foil on a bar coater with a thickness of 400 μm using the doctor blade method. The electrodes were dried in a vacuum oven at 80 ̊C overnight and further punched into 20 mm diameter discs. Additionally, punched electrodes were dried in a Büchi oven under vacuum at 120 ̊C overnight inside the glove-box. The loading of active material for the galvanostatic cycling was approximately 4-5 mg cm^{-2} after drying. Pouch cells were assembled in an argon filled glove-box using glass fiber membrane (Whatman®, 26 mm diameter, 240 μm thick) as separators, 22 mm of Na disks punched from metallic Na cubes (Sigma-Aldrich®) serving as the counter and reference electrode, and 200-250 μL of 1 M $NaPF_6$ (Stella, 99%) in diethylene glycol dimethyl ether (diglyme) (Sigma-Aldrich®, ≥99.99%) as the electrolyte.

2.4 Electron Microscopy

Field-emission scanning electron microscopy (FE-SEM) with energy dispersive X-ray (EDX) analysis was conducted using a Zeiss 1550 SEM operated at 5.0 kV to examine sample morphology, particle size, and elemental distribution. Powdered samples were mounted on aluminum stubs with carbon tape. Transmission electron microscopy (TEM) was performed using a Thermo Fisher Themis Z double aberration-corrected microscope, equipped with a Super-X EDS detector. Samples were crushed and dispersed directly onto Cu TEM grids with holey carbon films. The microscope operated at 300 kV, with fifth-order aberration correction, a convergence angle of 21 mrad, and probe current of 120 pA. High-angle annular dark-field (HAADF) and bright-field (BF) STEM imaging were used to analyze particle size, porosity, and elemental distribution. HAADF images were collected using a Fischione ADF detector (collection angle: 63–200 mrad) and BF images with a Thermo Fisher BF detector (angle: <35 mrad). Data acquisition and analysis were performed using Thermo Fisher Velox software

2.5 X-ray Powder Diffraction

X-ray powder diffraction (XRD) was used to determine the crystal structure and purity of the doped NFPP samples, respectively, using Bruker D8 Twin-Twin diffractometer equipped with a Cu Kα (λ = 1.5406 Å) source operated at 40 kV and 40 mA over the range of 5-70 ̊ (2Θ) with a scanning step of 0.01 ̊ s^{-1}. The refinement was performed using the Rietveld method [6] with the TOPAS software [7].

2.6 Raman Spectroscopy

Raman spectroscopy measurements were carried out by a Raman microscope (Renishaw-inVia) using an excitation wavelength of 532 nm generated by a laser diode (Renishaw) with a maximum output power of 100 mW. The laser beam was focused onto the surface of the K^+-NFPP and K^+-NFPP@rGO powder samples through a 50× objective. Prior to the measurements, instrument calibration was performed via monocrystalline Si to obtain a reference peak at ~520 cm^{-1}. The analyses consisted of subsequent extended spectral acquisitions between 200 and 3800 cm^{-1} with an acquisition duration of 30 s and a series of 50 accumulations to enhance the signal-to-noise ratio (S/N) of the spectra. A low laser power of 0.5% was employed during the measurements to prevent possible degradation of the sample surface and beam exposure minimization was also applied in between consecutive acquisitions. Baseline correction of the resulting spectra was performed via the dedicated function in the software Wire 4.4.

2.7 X-ray Photoelectron Spectroscopy

The valence and chemical states of different species present in as-prepared K-NFPP and K-NFPP@rGO were analyzed using a Kratos AXIS Supra+ X-ray photoelectron spectrometer. The spectra were obtained using a monochromatic Al Kα (1486.6 eV) source and calibrated by setting the C 1s (sp^3) species to a binding energy of 285 eV. The data was deconvoluted using CasaXPS software. A Shirley-type background and a peak shape of GL(30) were used during the analysis.

2.8 X-ray Absorption Spectroscopy

Fe K-edge XAS (XANES and EXAFS) was performed ex situ at beamline P64 of DESY (Hamburg, Germany). X-rays were monochromatized using a Si(111) double-crystal monochromator and focused to a 1 × 2 mm² spot. Samples were mounted at 45°, and fluorescence data were collected using a PIPS detector, while transmission data were acquired using ion chambers. Energy calibration was done using Fe metal foil. The chemical shifts (ΔE_0) were extracted from the first derivative of XANES, and Fe valence was estimated by comparison with standard reference oxides. EXAFS oscillations extended to $k \approx 12$ Å^{-1}, with data processed using Athena–Artemis software [8]. Soft XAS and RIXS measurements were conducted at beamline BL27SU of SPring-8 (Japan), with high resolution ($E/\Delta E > 10^4$) and photon flux (~10^{11} photons/s). A focused beam (10 × 200 μm²) was incident at 45°, with data collected in PFY and IPFY modes using a silicon drift detector (SDD) to minimize self-absorption. RIXS spectra were recorded using a cylindrical grating spectrometer with a CCD detector, achieving resolutions of ~1000 at the O K-edge and 600 at 1 keV [9]. All XAS spectra were normalized for inter-sample comparison.

2.9 Electrochemical Measurements

The electrochemical performance of pristine NFPP, Mn-NFPP, Ni-NFPP, Zn-NFPP and K-NFPP@rGO cathodes were investigated in pouch cells assembled in an Ar-filled glovebox in which O_2 and H_2O levels were below 1 ppm. The galvanostatic charge-discharge cycling measurements of half-cells were carried out using a Neware battery tester BTS4000 in a potential window of 1.8–3.8 V vs. Na/Na^+ at 25 ℃ after 12 h rest time to ensure proper wetting of electrodes. The carbon content within the carbon coated NFPP composites were excluded to calculate the specific capacities for each cell. The cyclic voltammetry (CV) tests were performed by using a Bio-Logic® MPG2 potentiostat.

3. Results and Discussion

3.1 Structure and Morphology of $Na_4Fe_{3-x}M_x(PO_4)_2(P_2O_7)$, (M: Mn^{2+}, Ni^{2+}, Zn^{2+})

$Na_4Fe_{3-x}Mn_x(PO_4)_2(P_2O_7)$ (x = 0.05, 0.1, 0.2 and 0.4) (NFMPP), $Na_4Fe_{3-x}Ni_x(PO_4)_2(P_2O_7)$ (x = 0.05, 0.1, and 0.2) (NFNPP) and $Na_4Fe_{3-x}Zn_x(PO_4)_2(P_2O_7)$ (x = 0.01, 0.03, 0.05, and 0.1) (NFZPP) were successfully prepared by a traditional sol-gel method involving a low-temperature calcination at 500 ºC under Ar or Ar/H_2 flow depending on the purity of compounds. XRD was used to determine the effect of different amount of Mn^{2+}, Ni^{2+}, and Zn^{2+} on the crystal structure and purity of NFPP as shown in **Figure 2**.

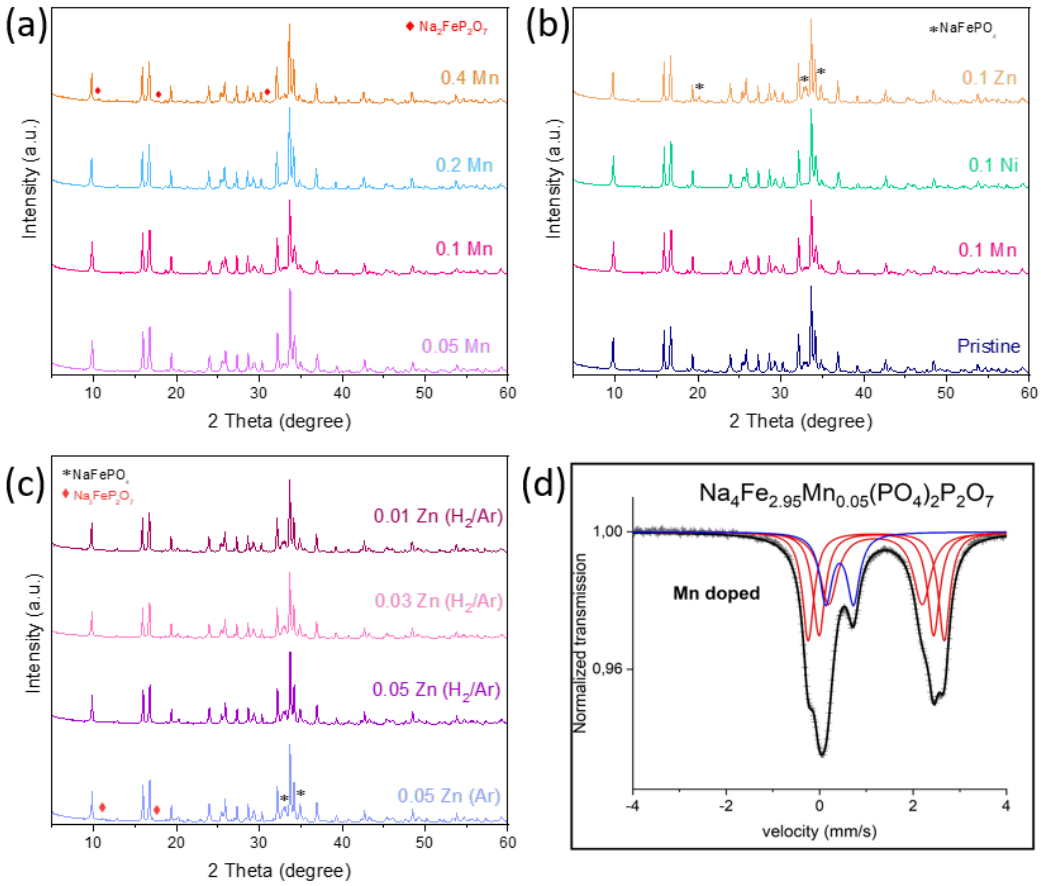

Figure 2. XRD patterns of (a) $Na_4Fe_{3-x}Mn_x(PO_4)_2(P_2O_7)$ (x = 0.05, 0.1, 0.2, and 0.4), (b) comparison of pristine, Mn, Ni, Zn doped NFPP, (c) $Na_4Fe_{3-x}Zn_x(PO_4)_2(P_2O_7)$ (x = 0.01, 0.03, and 0.05), and (d) Mössbauer spectra of the Mn doped samples of $Na_4Fe_3(PO_4)_2(P_2O_7)$, representative also for Ni and Zn dopants. The red and blue marked resonance lines represent high spin Fe^{2+} and Fe^{3+} valences.

All doped samples retained the orthorhombic crystal structure (space group $Pn2_1a$), confirming that low levels of metal-ion doping did not significantly alter the NFPP framework. Mn^{2+} doping at concentrations of x = 0.05 to 0.2 effectively reduced the intensity of the impurity peak associated with electrochemically m-$NaFePO_4$ suggesting improved phase purity and structural stability. However, higher Mn content (x = 0.4) led to the appearance of $Na_2FeP_2O_7$ impurity peaks, indicating a threshold above which structural distortion occurs.

Similar trends were observed for Ni doping. The 0.1 Ni-NFPP sample exhibited the highest crystallinity and lowest m-$NaFePO_4$ content, suggesting that Ni^{2+} is well tolerated within the NFPP lattice. In contrast, Zn doping introduced a higher concentration of both m-$NaFePO_4$ and $Na_2FeP_2O_7$ impurities, especially at x = 0.1, likely due to lattice destabilization. To mitigate this, a lower Zn doping range (x = 0.01–0.05) was explored. The choice of calcination atmosphere also played a significant role: a reducing Ar/H_2 (95:5) atmosphere reduced impurity content more effectively than inert (Ar) gas flow, likely due to partial reduction of Fe^{3+} and transformation of phosphate groups.

Rietveld refinement of selected doped NFPP compositions confirmed orthorhombic symmetry, with refined unit cell volumes of 1260.19 $Å^3$ (0.05 Mn-NFPP), 1258.52 $Å^3$ (0.1 Ni-NFPP), and 1261.97 $Å^3$ (0.05 Zn-NFPP). The slight decrease in volume for Ni-doped samples reflects the smaller ionic radius of Ni^{2+} (0.69 Å) compared to Fe^{2+} (0.78 Å). Mn and Zn doped samples showed nearly unchanged

volumes due to their similar ionic radii to Fe^{2+} and low doping levels. Quantitatively, the m-$NaFePO_4$ impurity content decreased from 10.74% in pristine NFPP to 4.10% in 0.1 Ni-NFPP and 7.99% in 0.05 Mn-NFPP, while it increased to 13.18% in 0.05 Zn-NFPP as shown in **Figure 3**.

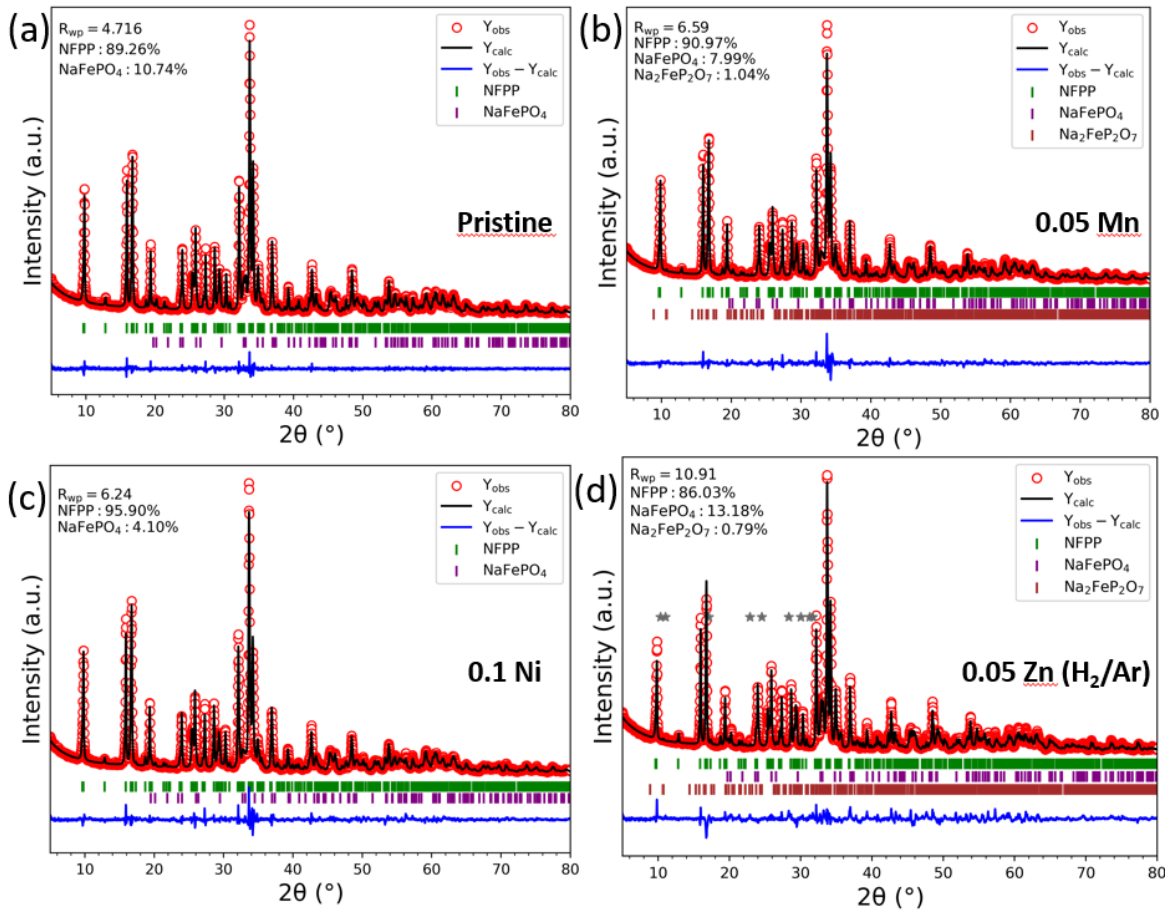

Figure 3. Rietveld refinement of the XRD pattern of the (a) pristine NFPP, (b) 0.05 Mn-NFPP, (c) 0.1 Ni-NFPP, and (d) 0.05 Zn-NFPP calcinated under reducing atmosphere. Vertical bars represent the Bragg positions for NFPP, maricite $NaFePO_4$, and $Na_2FeP_2O_7$.

Morphological characterization by SEM and TEM revealed that all samples consisted of irregularly shaped primary particles (**Figure 4**).

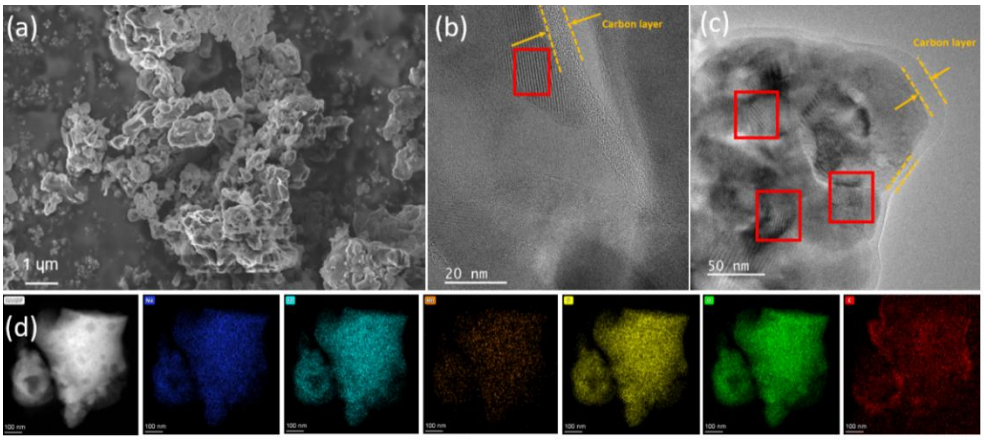

Figure 4. (a) SEM image of 0.1 Ni-NFPP, (b) HRTEM of Ni-NFPP, (c) HRTEM of Mn-NFPP, (d) HAADF- and BF-STEM images and (e) HAADF-STEM image and corresponding EDS mapping results of Mn-NFPP.

Doping with optimal concentrations of Mn and Ni led to smaller, more uniform particles and reduced agglomeration, resulting in a more interconnected and nanoporous structure. These features are favorable for Na^+ diffusion and contribute to improved electrochemical performance. EDX elemental mapping confirmed homogeneous distribution of Na, Fe, P, O, and C, particularly in Mn-NFPP. Furthermore, a homogeneous amorphous carbon layer was observed on the surface of Mn- and Ni-doped particles, which is expected to improve surface electronic conductivity.

3.2 Structure and Morphology of K^+ doped $Na_{4-x}K_xFe_3(PO_4)_2(P_2O_7)$@rGO Composite

The crystal structures of $Na_{4-x}K_xFe_3K_x(PO_4)_2(P_2O_7)$@rGO samples were examined using XRD as shown in **Figure 5**.

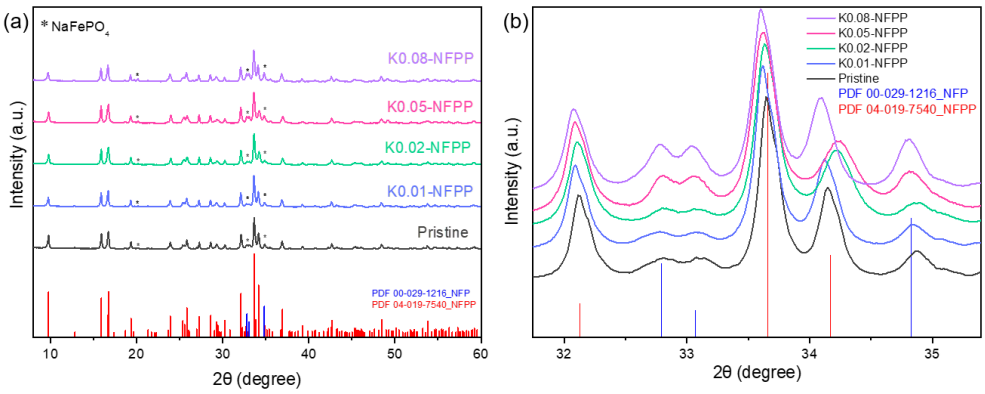

Figure 5. XRD patterns of pristine NFPP, K0.01-NFPP, K0.02-NFPP, K0.05-NFPP, K0.08-NFPP, measured using Cu Kα radiation (λ = 1.5406 Å), shown over the 2θ range of 8–60° (a) and 31.5–35.5° to show characteristic peaks of m-$NaFePO_4$.

All compositions retained the orthorhombic $Pn2_1a$ symmetry consistent with the standard NFPP phase (PDF 04-019-7540), confirming successful synthesis. The presence of sharp and well-defined peaks indicated that all samples were well-crystallized and structurally homogeneous. Lower potassium doping levels (K0.01 and K0.02) effectively suppressed the formation of this impurity, with K0.02NFPP displaying the highest phase purity. However, increased doping levels (K0.05 and K0.08) reintroduced

the m-$NaFePO_4$ phase, likely due to the destabilizing effect of the larger K^+ ionic radius (1.38 Å) on the NFPP lattice. This behavior aligns with earlier reports that associate excessive alkali doping with lattice distortion and defect formation, which can facilitate impurity stabilization. Peak shifts toward lower angles observed in all doped samples indicated lattice expansion resulting from K^+ incorporation. Since K^+ is electrochemically inactive, it serves as a structural stabilizer ("pillar") rather than a redox-active species. This expansion helps accommodate Na^+ diffusion by increasing the interstitial space within the host framework, which is beneficial for ionic transport during cycling. To further improve electronic conductivity and structural integrity, reduced graphene oxide (rGO) was incorporated into the optimum K0.02-NFPP composition. XRD comparison (**Figure 6a**) between K0.02-NFPP and K0.02-NFPP@rGO showed no significant changes to the host lattice, confirming that rGO does not substitute into the crystal structure. Instead, it forms a conductive surface coating. A broad diffraction peak at ~26.5° in the rGO composite confirmed the presence of graphitic carbon.

Raman spectroscopy revealed characteristic D (~1359 cm^{-1}) and G (~1591 cm^{-1}) bands in both materials (**Figure 6b**). The intensity ratio (I_D/I_G) was 0.70 for K0.02NFPP and 0.76 for K0.02NFPP@rGO, indicating a slightly higher degree of graphitization in the rGO-coated sample. This higher graphitic content is associated with improved electron transport and mechanical resilience, both of which are beneficial for battery cycling performance.

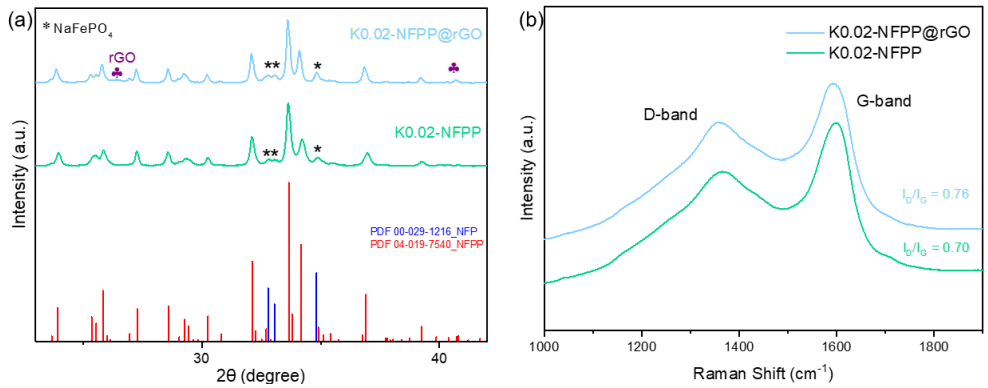

Figure 6. (a) Comparison of XRD pattern between K0.02-NFPP (shown in green) and K0.02-NFPP@rGO (shown in blue). (b)Raman spectra of K0.02-NFPP and K0.02-NFPP@rGO.

The XPS survey spectra of K0.02-NFPP and K0.02NFPP@rGO (**Figure 7a–b**) confirm the presence of C, P, K, Fe, Na, and O on the material surfaces. As shown in **Figures 7c–f**, both samples exhibit similar surface species in the C 1s and O 1s regions.

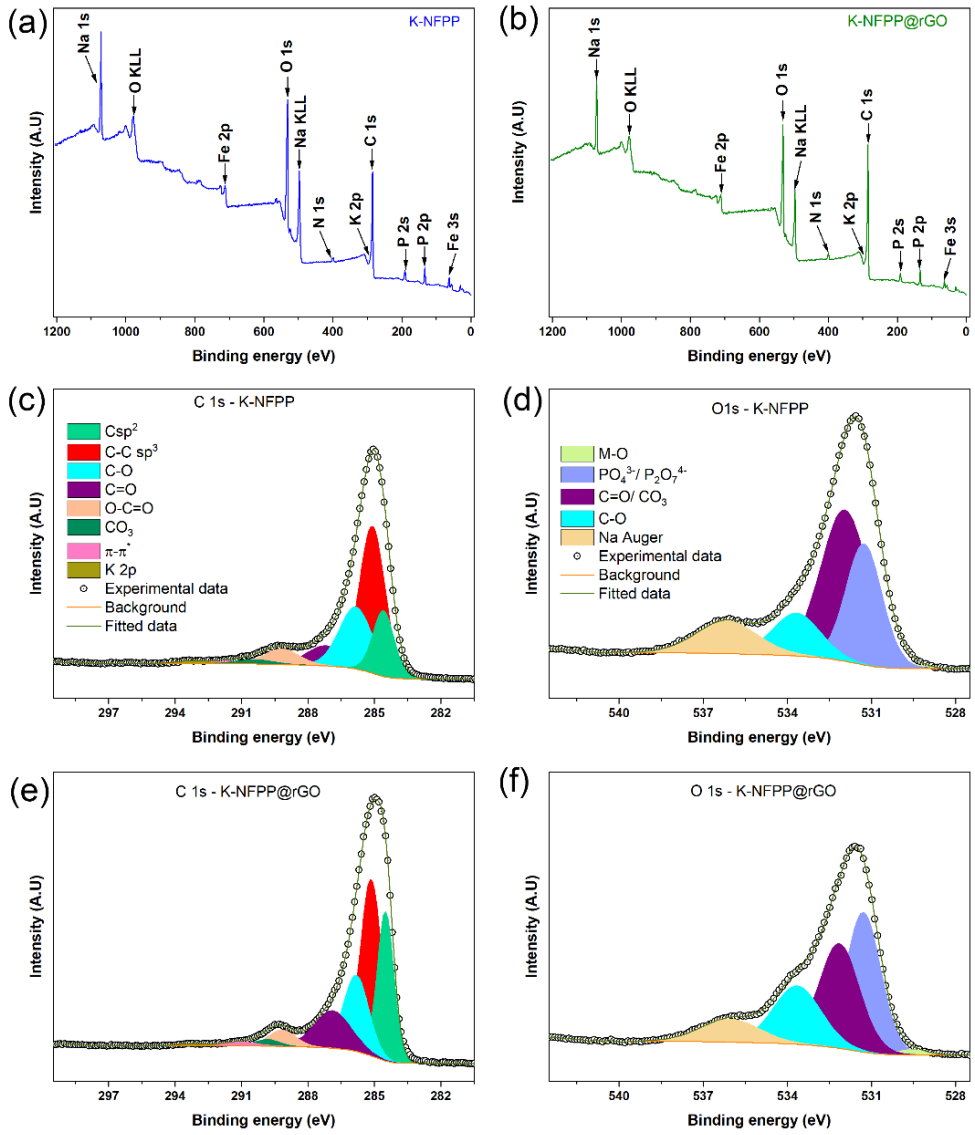

Figure 7. XPS analysis of K0.02-NFPP and K0.02-NFPP@rGO materials. a) and b) represent the survey spectra of K0.02-NFPP and K0.02NFPP@rGO, respectively. c), d) and e), f) correspond to the deconvoluted high-resolution XPS spectra of C 1s and O 1s regions of the analyzed raw materials.

The C 1s spectra include peaks corresponding to C–C (sp^2 ~284.6 eV), C–C (sp^3 ~285.1 eV), C–O (~285.8 eV), C=O (~287 eV), O–C=O (~289.1 eV), CO_3^{2-} (~290 eV), π→π (~291.1 eV), and K 2p (~293 eV)**. The sp^2 and sp^3 carbon species are likely formed during annealing, while oxygenated carbon groups (C–O, C=O, O–C=O, CO_3^{2-}) may arise from atmospheric exposure or residual synthesis byproducts. The π→π peak is attributed to graphitic carbon, and its enhanced intensity in K0.02-NFPP@rGO indicates successful rGO surface modification, consistent with literature [10]. Although K^+ detection is challenging due to low doping levels and carbon surface coverage, a minor intensity increases at ~293 eV is attributed to K 2p, as no fluorine is present to cause overlap (e.g., C–F_x species). In the O 1s region, peaks are observed for M–O (~529.6 eV), P–O (~531.3 eV, from PO_4^{3-} and $P_2O_7^{4-}$ units), C=O/CO_3^{2-} (~532 eV), and C–O (~533.6 eV). A broader feature around 536 eV corresponds to a Na Auger signal, in agreement with previous reports [11].

SEM showed that pristine K0.02-NFPP consisted of relatively dense, irregular particles, while the rGO-coated sample exhibited a more porous network formed by overlapping graphene nanosheets (**Figure 8**).

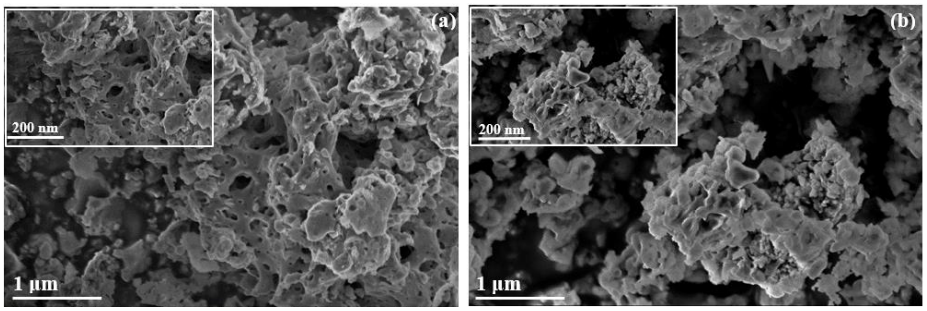

Figure 8. Morphological analysis, SEM images of (a) K0.02-NFPP@rGO (b) K0.02-NFPP

Both materials consisted of < 200 nm primary particles and secondary agglomerates in the micron range. The porous architecture in the rGO composite provides a higher surface area and more accessible pathways for Na^+ transport.

3.3 Electrochemical Performance of $Na_4Fe_{3-x}M_x(PO_4)_2(P_2O_7)$

To evaluate the effect of Mn^{2+}, Ni^{2+}, and Zn^{2+} doping on the electrochemical behavior of NFPP cathodes, galvanostatic charge-discharge cycling and CV were conducted in half-cells within a voltage window of 1.8–3.8 V (**Figures 9–10**).

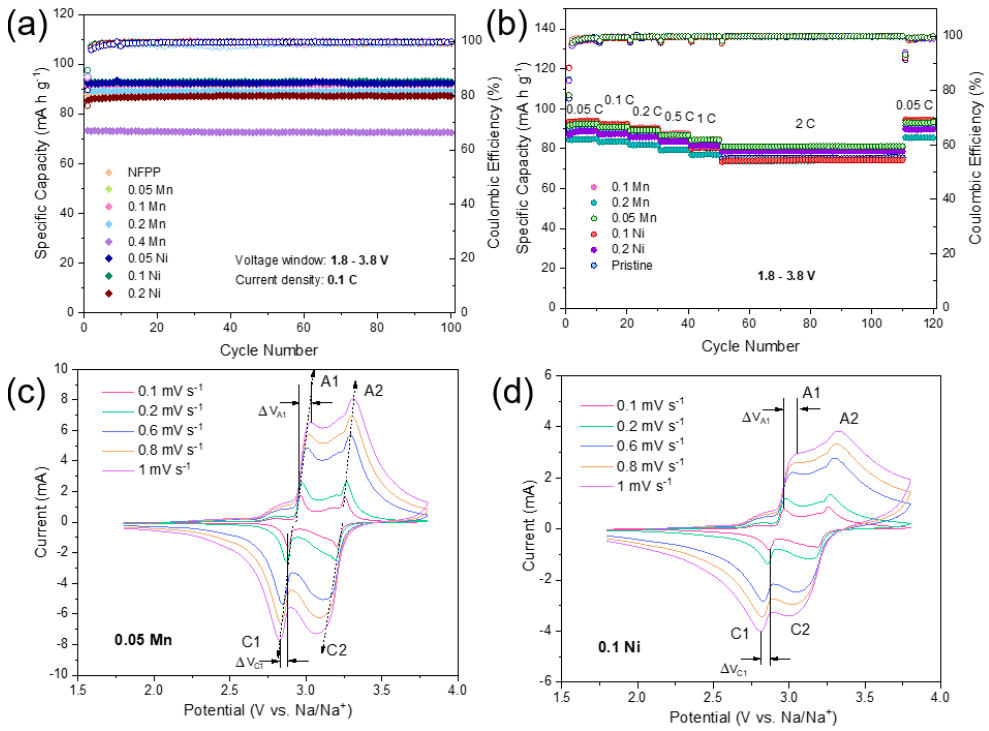

Figure 9. (a) Capacity retention at 0.1 C and corresponding Coulombic efficiencies for 100 cycles, (b) rate capability at various current rates from 0.05 C to 2 C of Mn and Ni doped NFPP in half-cells, (c,d) CV curves at various scan rates from 0.1 to 1 mV s^{-1} of $Na_4Fe_{2.95}Mn_{0.05}(PO_4)_2(P_2O_7)$, $Na_4Fe_{2.9}Ni_{0.1}(PO_4)_2(P_2O_7)$.

Long-term cycling was performed at 0.1 C (1 C = 129 mAh g^{-1}). The pristine NFPP exhibited initial charge and discharge capacities of 100 and 88 mAh g^{-1}, respectively, with a coulombic efficiency (CE) of 87%. Carbon content (~11%) was excluded from capacity calculations, as in-situ carbon was not electrochemically active. Among Mn-doped samples, 0.4 Mn-NFPP delivered a lower capacity of 74 mAh g^{-1}, likely due to excess Mn^{2+} introducing structural distortion and deteriorating performance. In contrast, the optimized 0.05 Mn-NFPP achieved 91 mAh g^{-1} discharge capacity. For Ni-doped samples, 0.1 Ni-NFPP outperformed the 0.2 Ni composition, providing a reversible capacity of 92 mAh g^{-1} compared to 86 mAh g^{-1}. After 100 cycles, 0.05 Mn-NFPP and 0.1 Ni-NFPP showed excellent stability with capacity retentions of 99.80% and 99.76%, and initial CE values of 87% and 89%, respectively (**Figure 9a**). Rate performance tests (**Figure 9b**) showed that 0.05 Mn-NFPP retained higher capacities than 0.1 Ni-NFPP across increasing C-rates. At 0.05 to 2 C, the Mn-doped sample delivered 92, 91, 89, 84, and 81 mAh g^{-1}, while the Ni-doped sample produced 94, 92, 89, 83, 80, and 74 mAh g^{-1}. When returned to C/20 after 110 cycles, both samples recovered their initial capacities (~93–94 mAh g^{-1}), confirming their structural reversibility. Notably, 0.05 Mn-NFPP exhibited superior high-rate performance, maintaining higher capacity at 2 C compared to Ni-doped NFPP.

CV measurements at scan rates from 0.1 to 1 mV s^{-1} (**Figure 9c–d**) revealed two redox peak couples for both doped samples: 2.96/2.88 and 3.25/3.20 V for 0.05 Mn-NFPP; 2.97/2.87 and 3.26/3.18 V for 0.1 Ni-NFPP. These peaks correspond to the reversible Fe^{3+}/Fe^{2+} redox reactions and Na^+ intercalation at different sites. A small peak at ~2.80 V appearing after the first charge is attributed to structural rearrangement. As scan rate increased, anodic peaks shifted positively and cathodic peaks negatively, indicating polarization effects. 0.05 Mn-NFPP showed higher redox peak intensity and more symmetrical profiles, suggesting better reversibility and faster Na^+ diffusion compared to 0.1 Ni-NFPP. These observations were consistent with differential capacity (dQ/dV) analysis (**Figure 10e**), which also supported enhanced redox kinetics and structural stability for the Mn-doped sample.

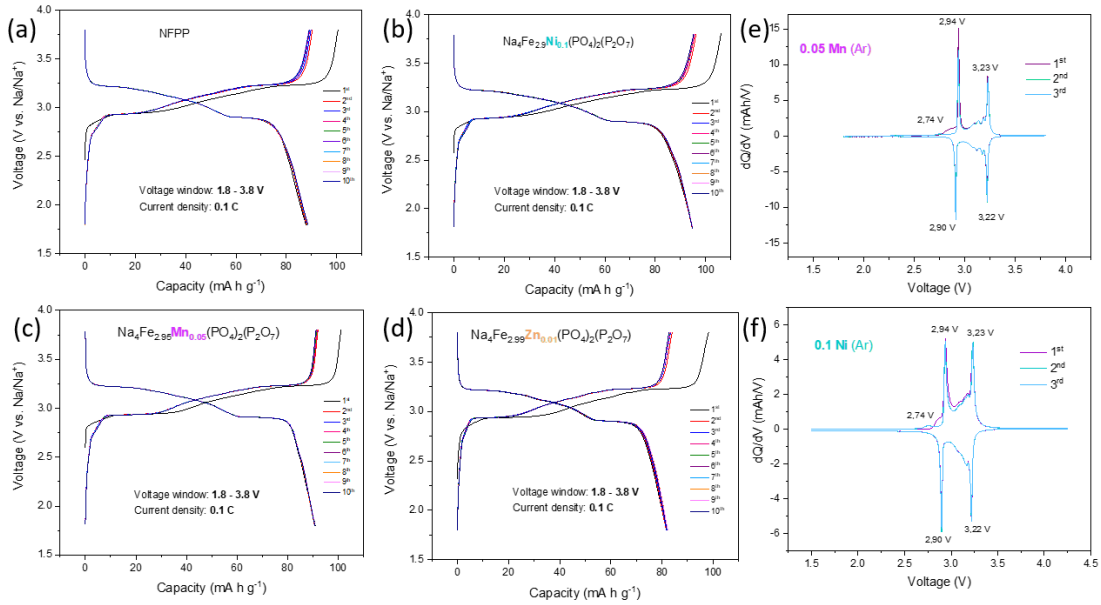

Figure 10. The first ten charge−discharge curves of (a) pristine NFPP, (b) 0.1 Ni, (c) 0.05 Mn, and (d) 0.01 Zn, (e,f) corresponding differential capacity vs. voltage (dQ/dV) plots for 3 cycles of 0.05 Mn and 0.1 Ni sample.

The sample 0.1 Zn doped calcinated under Ar atmosphere exhibited the lowest discharge capacity of 63 mAh g^{-1}, attributed to excessive Zn^{2+} doping, which likely caused structural distortion and the formation

of electrochemically inactive $Na_2ZnP_2O_7$. When a reducing H_2/Ar atmosphere was used during calcination, the electrochemical performance improved. Specifically, 0.05 Zn, 0.03 Zn, and 0.01 Zn (H_2/Ar) delivered capacities of 80, 81, and 82 mAh g^{-1}, respectively, at 0.1C, though still lower than pristine NFPP (88 mAh g^{-1}). Among these, 0.01 Zn (H_2/Ar) showed the best performance, with an initial CE of 83% (**Figure 10d**) and 98.91% capacity retention after 100 cycles, with an average CE of 99.4%. The improved capacity under reducing conditions is likely due to a lower impurity content compared to samples calcinated under Ar flow. Inferior capacities were obtained for all Zn doped samples. Zn^{2+} substitution led to formation of 1% excess Na content in addition to the Fe deficiency within 0.05 Zn-NFPP in good accordance with higher m-$NaFePO_4$ and $Na_2ZnP_2O_7$ amounts in Zn doped samples, thus worsening Na^+ diffusion kinetics and conductivity [12].

3.4 Electrochemical Performance of K^+ doped $Na_{4-x}K_xFe_3(PO_4)_2(P_2O_7)$@rGO Composite

Galvanostatic charge-discharge tests (**Figure 11**) revealed that K^+ doping improves the electrochemical performance of NFPP, with K0.02-NFPP delivering the highest reversible capacity of 98.31 mAh g^{-1} at 0.05C, compared to pristine and other doped NFPP samples. Doping at lower levels effectively suppressed maricite formation, increasing the number of electrochemically active sites. The incorporation of reduced graphene oxide (rGO) in K0.02-NFPP led to enhanced rate capability, achieving 88.83 mAh g^{-1} at 2C (**Figure 12a**), attributed to improved electronic conductivity through the 3D carbon network.

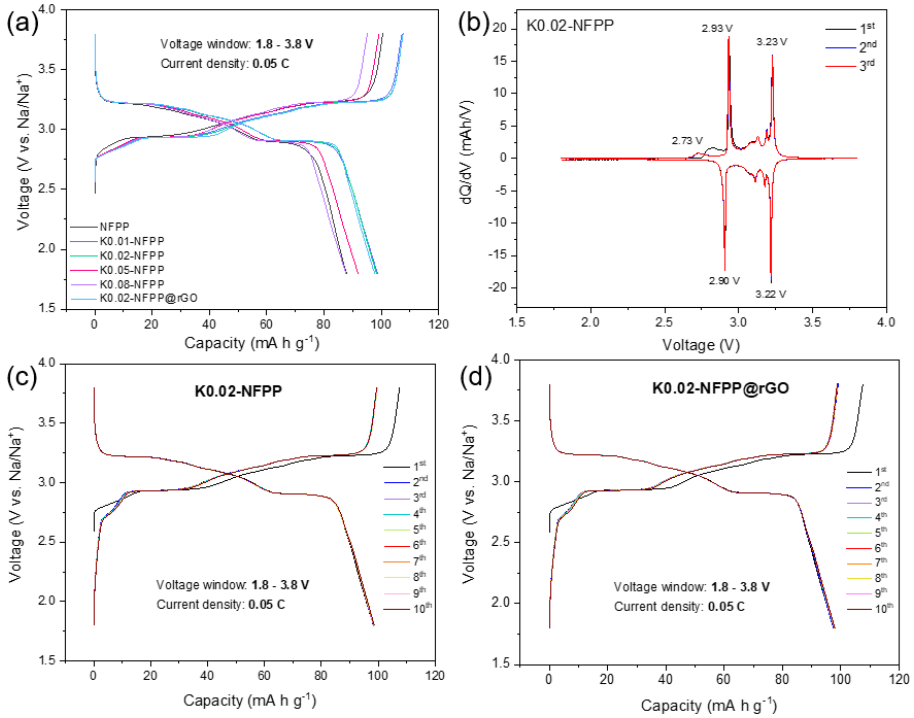

Figure 11. (a) Initial charge-discharge profiles of NFPP, K0.01-NFPP, K0.02-NFPP, K0.05-NFPP, K0.08-NFPP, K0.02-NFPP@rGO (b) dQ/dV vs Voltage profile of 3 cycles from K0.02-NFPP (c) initial ten charge-discharge profile at 0.05C of K0.02-NFPP and (d) K0.02NFPP@rGO.

In rate capability tests (**Figure 12a**), K^+-doped samples outperformed pristine NFPP at nearly all rates. Although K0.02-NFPP showed slightly higher capacity than K0.02-NFPP@rGO at low C-rates, the rGO-containing material outperformed at high rates, demonstrating the benefits of enhanced ionic conductivity. All samples recovered their initial capacity after returning from 2C to 0.05C, confirming structural stability. As shown in **Figure 12b**, K0.02-NFPP retained 98.07% of its capacity, while K0.02-

NFPP@rGO achieved a capacity retention of 99.4% after 1000 cycles at 2C, highlighting their excellent durability and the effectiveness of K^+ doping and rGO in enhancing both stability and high-rate performance.

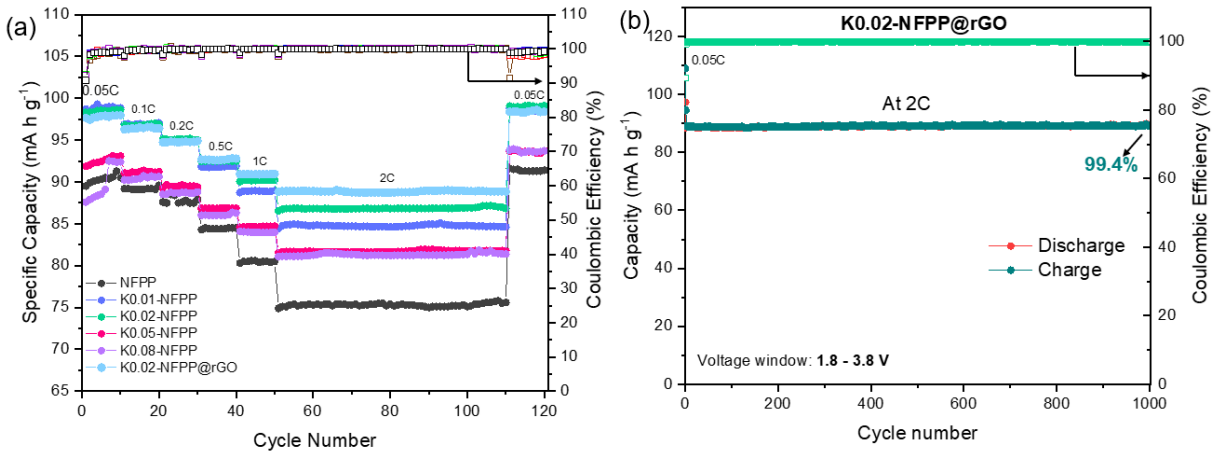

Figure 12. (a) Rate capability test of different scan rates from 0.05C to 2C of NFPP, K0.01-NFPP, K0.02-NFPP, K0.05-NFPP, K0.08-NFPP, K0.02-NFPP@rGO. (b) Long-term cycling performance of K0.02-NFPP@rGO at 2C.

3.5 X-ray Absorption Spectroscopy (XAS) and Resonant Inelastic X-ray Scattering (RIXS) Measurements

XAS and RIXS were used to investigate redox behavior and local structural changes in pristine and optimum doped NFPP materials. **Figure 13(a)** shows Fe K-edge XANES spectra for pristine NFPP at different cycling states.

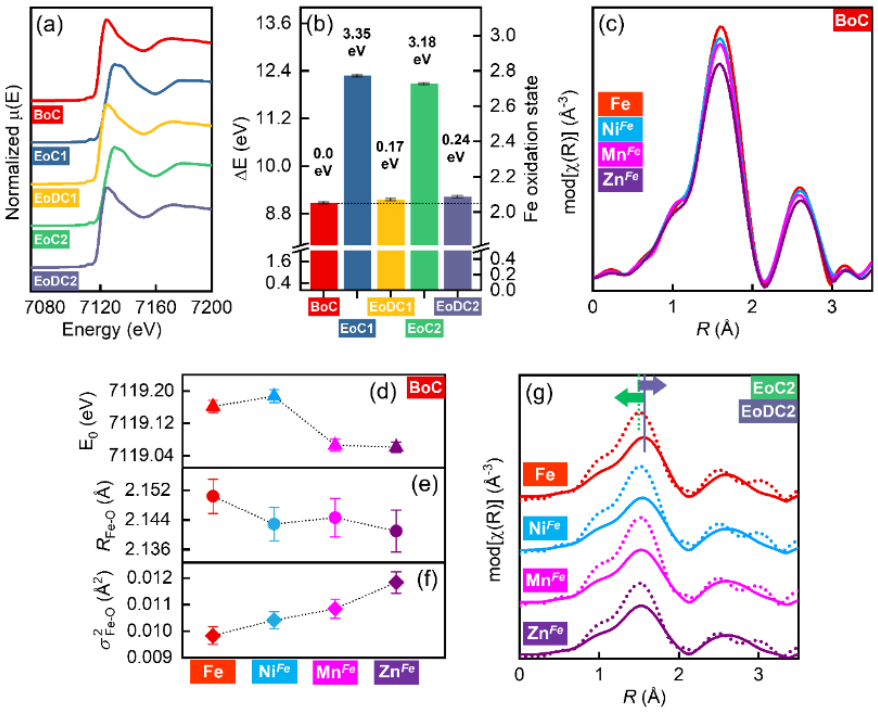

Figure 13. (a) Normalized Fe *K*-edge XANES collected ex-situ for undoped NFPP cathodes at BoC (red), EoC (dark blue) and EoDC (yellow) for the 1st cycle, EoC (green) and EoDC (dark purple) for the

2nd cycle. (b) Reversible $Fe^{2+} \leftrightarrow Fe^{3+}$ redox detected from chemical shifts of Fe 1*s* core level binding energies at respective charging states. (c) Comparative Fe EXAFS (modulus of $\chi(R)$) of NFPP electrodes: undoped (red), doped with Ni (cyan), Mn (magenta) and Zn (purple). (d) Characteristic dopant-induced changes on Fe chemistry in terms of Fe redox and local bonding arrangements around Fe sites in terms of (e) Fe-O bond lengths and (f) Fe-O local disorder. (g) Reversible local structural relaxations about Fe atoms in pristine NFPP, Mn-NFPP, Ni-NFPP, Zn-NFPP.

The absorption edge (E_0) shifts to higher energies during charging and returns upon discharging, confirming a highly reversible Fe^{2+}/Fe^{3+} redox process. ΔE_0 values (**Figure 13b**) suggest that Fe is predominantly Fe^{2+} at the beginning of charge and effectively reverts after discharge, consistent with CV results. **Figure 13(c)** compares Fe K-EXAFS (χ(R)) of pristine NFPP with Ni-, Mn-, and Zn-doped NFPP. All maintain similar structural features, indicating the rigidity of the NFPP lattice, though doping introduces local disorder, especially in Zn-doped samples, as reflected by reduced EXAFS amplitudes. From **Figure 13(d–f)**, E_0 values remain close to Fe^{2+} for all doped samples, indicating isovalent substitution. Fe–O bond lengths (R_{Fe-O}) slightly decrease, while bond disorder (σ^2_{Fe-O}) increases with doping, especially for Zn. These changes arise from size mismatch between dopants and Fe, with Zn inducing the most distortion, correlating with performance loss at higher doping levels. Overall, Ni introduces the least structural distortion. **Figure 13(g)** further shows that charging increases local order around Fe due to Fe–O bond compression (~0.05 Å), which reverses upon discharge demonstrating reversible structural relaxation linked to Na^+ migration.

XAS at the O K-edge and Fe L-edge was performed on Mn-, Ni-, and Zn-doped NFPP (**Figure 14a–b**).

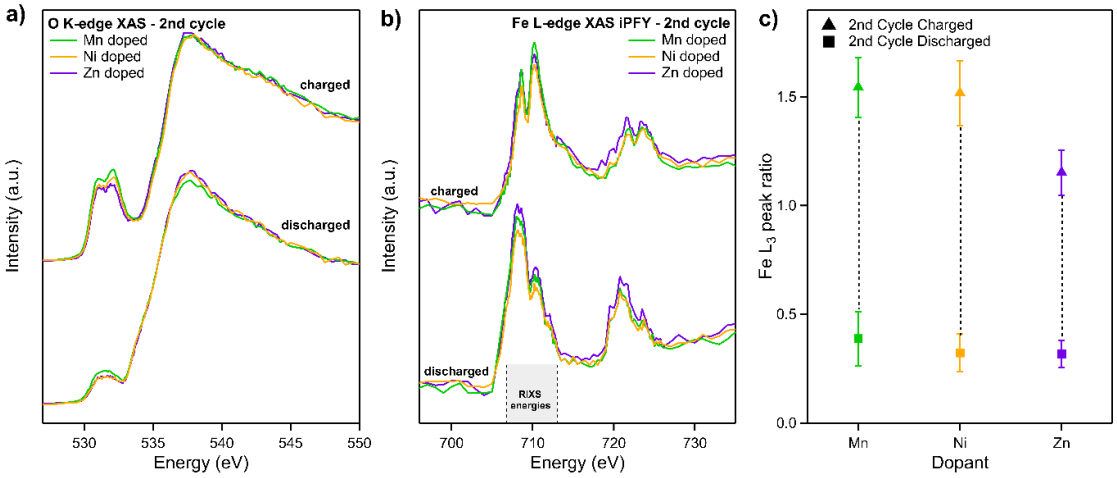

Figure 14. The a) O K-edge TFY XAS and b) Fe L-edge iPFY XAS of the Mn-, Ni- and Zn-NFPP cathodes in the second cycle charged (top) and discharged (bottom) state. In c) the area ratio of the 707 - 709.5 eV peaks to the 709 - 713.5 eV peaks in b) is displayed as triangles for the charged cathodes and squares for the discharged ones.

The pre-edge region (529.5–533.5 eV) reflects Fe–O hybridization, with Mn-NFPP showing the highest pre-peak intensity, indicating strongest Fe–O orbital overlap. Upon charging, pre-peak intensities increase for all samples, with Mn > Ni > Zn, suggesting higher oxygen redox contribution in Mn- and Ni-doped samples. Fe L-edge spectra (**Figure 14b**) show that all cathodes return to Fe^{2+} after discharge. Upon charging, Mn- and Ni-doped NFPP reach oxidation states closer to Fe^{3+} than Zn-NFPP, confirming more complete charge compensation. **Figure 14(c)** presents Fe L_3 intensity ratios, again showing Mn-NFPP has the most pronounced Fe oxidation upon charge. This aligns with its superior capacity and

structural reversibility. Fe L_3-edge RIXS maps (**Figure 15**) for Mn-, Ni-, and Zn-doped NFPP reveal similar spectral structures dominated by dd-excitations.

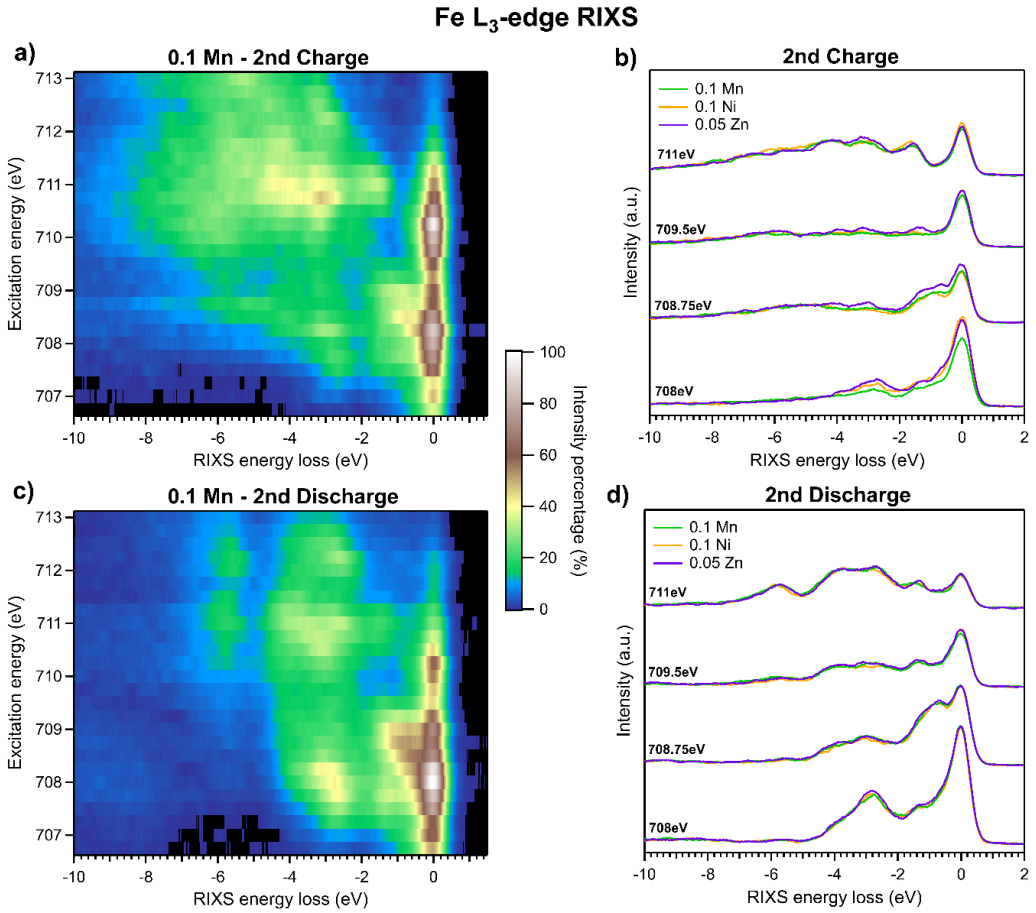

Figure 15. Fe L3-edge RIXS maps of Mn-NFPP in the second cycle a) charged and c) discharged state. b) and d) display selected spectra from a) and c), respectively.

Zn-doped NFPP shows stronger dd-features, indicating greater charge localization in the Fe d-band. This suggests poorer charge mobility, likely contributing to the inferior performance of Zn-doped samples.

4. Conclusions

This work provides valuable insight into the synergistic effects of alkali metal doping (Mn^{2+}, Ni^{2+}, Zn^{2+}, K^{+}) and carbon modification with rGO, offering a promising strategy for developing high-performance SIB cathodes using a simple and cost-effective synthesis methods. It advances the understanding of how lattice modifications affect ion diffusion and charge compensation, laying the foundation for more efficient and sustainable SIB technologies. Additionally, Mn- and Ni-doped NFPP composites were developed to further explore defect-induced conductivity enhancement. 0.05 Mn-NFPP, with 10% Fe and 1% Na vacancies, exhibited improved capacity, rate performance, and cycling stability due to suppressed maricite content and enhanced Na^{+} mobility. 0.1 Ni-NFPP maintained highest phase purity but showed performance limitations at higher C-rates. Ex situ XAS analyses revealed that doping introduces local lattice distortions, with Ni causing the least disruption. All samples exhibited highly reversible $Fe^{2+} \leftrightarrow Fe^{3+}$ redox behavior, with Fe–O bond length changes reflecting structural resilience

during cycling. O K-edge XAS showed the strongest Fe–O hybridization in Mn-NFPP, reinforcing its superior performance.

K^+ doping effectively suppressed maricite formation and expanded the lattice. Among the doped materials, K0.02-NFPP achieved the highest reversible capacity of 98.31 mAh g^{-1} at 0.05C, while K0.02NFPP@rGO reached 88.83 mAh g^{-1} at 2C, highlighting improved rate capability. The material also showed excellent stability with 99.4% capacity retention after 1000 cycles. Further improvement of the capacity can be achieved by the optimization of rGO amount to enhance both mechanical integrity and electron flow to active sites providing more uniform Na^+ diffusion across the electrode.

Project Outcomes

Three manuscripts have been prepared based on the findings of this project, highlighting the promising results of the doped NFPP/rGO composites. Some of the results of this project were presented at 2025 Materials Research Society (MRS) Spring Meeting. These results will be published in scientific articles in the coming months.

Acknowledgements

Subaşı is grateful to ÅForsk for financially supporting this project and to Pontus Törnblom, Moritz Hirsbrunner, Soham Mukherjee for performing ex-situ X-ray absorption spectroscopy (XAS) and resonant inelastic X-ray scattering (RIXS) measurements and analysis of the results. Reza Younesi and Haidong Liu are also thanked for his assistance in the project and valuable discussions. StandUp for Energy and Swedish Energy Agency are acknowledged for the financial support to the project "X-ray based methodology for next generation Na-ion battery cathodes" to the Department of Physics. Mochammed Luthfi Hamdani for performing the experiments on K^+-NFPP@rGO composite as a master thesis project.

Financial Reporting

The following Table gives an overview of the financial status of the project. After getting a travel grant from Wenner-Gren Foundations, some of the results of this project were disseminated at 2025 MRS Spring Meeting (EN02 Sodium Based Energy Storage). Large proportion of the costs were made towards salary.

Budget (SEK)	
Salary (6 months full time)	335 434
Material	4 674
Other costs	6 045
Overhead	103 846
Total project costs	**450 000**

References

[1] J. Gao, Y. Mei, L. Ni, H. Wang, B. Song, W. Deng, G. Zou, H. Hou, X. Ji, Inorganic Chemistry 2023, 62, 9099-9110.
[2] X. Wu, G. Zhong, Y. Yang, Journal of Power Sources 2016, 327, 666-674.
[3] Y. Cao, X. Xia, Y. Liu, N. Wang, J. Zhang, D. Zhao, Y. Xia, Journal of Power Sources 2020, 461, 228130.
[4] J. Gao, H. Chen, Y. Mei, L. Ni, H. Wang, J. Huang, N. Hong, B. Song, Y. Tian, W. Deng, G. Zou, H. Hou, X. Ji, Nano Energy 2023, 115, 108747.
[5] R. Gond, S. S. Meena, S. M. Yusuf, V. Shukla, N. K. Jena, R. Ahuja, S. Okada, P. Barpanda, Inorganic Chemistry 2017, 56, 5918-5929.
[6] H. Rietveld, Acta Crystallographica 1967, 22, 151-152.
[7] A. A. Coelho, Journal of Applied Crystallography 2018, 51, 210-218.
[8] aB. Ravel, M. Newville, Journal of synchrotron radiation 2005, 12, 537-541; bS. Zabinsky, J. Rehr, A. Ankudinov, R. Albers, M. Eller, Physical Review B 1995, 52, 2995.
[9] Y. Takata, T. Tokushima, Y. Harada, N. Kamakura, Y. Kitajima, M. Nagasono, Y. Tamenori, H. Ohashi, A. Hiraya, E. Ishiguro, S. Shin, AIP Conference Proceedings 2004, 705, 1186-1189.
[10] T. Yuan, Y. Wang, J. Zhang, X. Pu, X. Ai, Z. Chen, H. Yang, Y. Cao, Nano Energy 2019, 56, 160-168.
[11] aJ. He, T. Tao, F. Yang, Z. Sun, ChemSusChem 2022, 15, e202200817; bN. Zhao, C. Li, X. Guo, Physical chemistry chemical Physics 2014, 16, 15646-15652.
[12] H. Dai, Y. Xu, Y. Wang, F. Cheng, Q. Wang, C. Fang, J. Han, P. K. Chu, ACS Applied Materials & Interfaces 2024, 16, 7070-7079.